





# Self-assembled uniform double-shelled $\text{Co}_3\text{V}_2\text{O}_8$ hollow nanospheres as anodes for high-performance Li-ion batteries

Hao Zheng, Xiao Chen, Yun Yang, Lin Li, Chuan-Qi Feng\* , Shi-Quan Wang\* 

Received: 17 June 2020 / Revised: 22 July 2020 / Accepted: 20 January 2021 / Published online: 9 March 2021  
© Youke Publishing Co., Ltd. 2021

**Abstract** Hollow micro-/nanostructures have achieved great success in the field of renewable battery materials by reducing the volume change and promoting the ion transport. Double-shelled  $\text{Co}_3\text{V}_2\text{O}_8$  hollow nanospheres (CVO-DSS) were synthesized using a facile solvothermal method followed by a thermal treatment in the absence of any surfactant. Meanwhile, two other architectures of hollow nanospheres and nanoparticles were obtained by changing the annealing temperature. Benefiting from the desired hollow structure, the CVO-DSS electrode exhibits excellent lithium storage properties as an anode. It exhibits a reversible discharge capacity of  $1210 \text{ mAh}\cdot\text{g}^{-1}$  at  $200 \text{ mA}\cdot\text{g}^{-1}$  after 100 cycles and a satisfactorily high rate capacity of  $628 \text{ mAh}\cdot\text{g}^{-1}$  after 800 cycles at  $5000 \text{ mA}\cdot\text{g}^{-1}$ . These hollow nanostructures can efficiently enhance the contact area of the electrolyte/electrode interface, promote the diffusion of lithium ions and electrons and slow down the capacity loss during long cycles.

**Keywords**  $\text{Co}_3\text{V}_2\text{O}_8$ ; Hollow nanospheres; Double-shelled; Anode materials; Electrochemical properties

## 1 Introduction

Nowadays, lithium-ion batteries (LIBs) are extensively applied in the industrial and commercial applications (such as laptops, mobile communication equipment and electric vehicles) [1, 2]. To meet the increasing demands of the industries, the energy density and the cycle life of LIBs need to be further improved. Hence, many anode materials with superior electrochemical properties were reported and replaced the traditional graphite anode [3–5]. Among these materials, binary cobalt vanadates (such as  $\text{Co}_3\text{V}_2\text{O}_8$ ) have attracted much attention as an alternative to oxide-based anodes owing to the presence of multivalent vanadium element, interfacial effects and synergistic effect of Co and V ions [6, 7]. However, the decrease in volume expansion and mechanical strength of bulk material can reduce the storage efficiency of lithium upon cycling and impede their use in the commercial applications.

Several approaches have been employed to overcome these issues such as rational fabrication and synthesis of nanostructured materials [8–12]. The nanostructured materials allow the electrolyte throughout the electrode, provide shorter diffusion path length, restrict the volume expansion and enhance the contact area [13–20]. Thus, a variety of micro-/nanostructured  $\text{Co}_3\text{V}_2\text{O}_8$  materials have been reported, such as nanotubes [21], hollow and solid hexagonal micro-pencils [22], mesoporous nanoparticles [23] and porous microspheres [24]. For example, the  $\text{Co}_3\text{V}_2\text{O}_8\cdot n\text{H}_2\text{O}$  hollow pencils exhibited impressive lithium storage capability, owing to their interfacial effects, multivalent vanadium ions and the reduction of volume expansion caused by the synergistic effects [25]. The multilayered  $\text{Co}_3\text{V}_2\text{O}_8$  nanosheets exhibited an outstanding specific capacity of  $470 \text{ mAh}\cdot\text{g}^{-1}$  at  $5.0 \text{ A}\cdot\text{g}^{-1}$  over 500

---

Hao Zheng and Xiao Chen have contributed equally to this work.

H. Zheng, L. Li  
Key Laboratory of Functional Materials and Chemistry for Performance and Resources of the Guizhou Education Department, Anshun University, Anshun 561000, China

X. Chen, Y. Yang, C.-Q. Feng\*, S.-Q. Wang\*  
Key Laboratory for Synthesis and Applications of Organic Functional Molecules, Hubei University, Wuhan 430062, China  
e-mail: cfeng@hubu.edu.cn

S.-Q. Wang  
e-mail: wsqhao@hubu.edu.cn

cycles, in which the reversible reaction of  $\text{Co}^{2+}/\text{Co}^0$  and  $\text{Li}_x\text{V}_2\text{O}_5$  acts as an electrochemical reaction, confirmed by ex situ transmission electron microscope (TEM). These nanosheets not only enhanced the contact area, but also assured favorable kinetics and a stable structure [26]. The porous  $\text{Co}_3\text{V}_2\text{O}_8$  nanosheets exhibited excellent lithium storage capacity. These layer-to-layer nanosheets with mesoporous structure and synergistic effect prevented the storage capacity from decaying and contributed in regaining the capacity [27]. Among various nanostructures, the hollow micro-/nanostructured electrodes have attracted remarkable attention due to the shorter diffusion path length and larger contact area [28, 29]. Luo et al. [30] recently synthesized interconnected  $\text{Co}_3\text{V}_2\text{O}_8$  hollow microspheres by a hydrothermal method followed by annealing; these microspheres displayed high cycling stability and rate capability ( $424 \text{ mAh}\cdot\text{g}^{-1}$  at  $10 \text{ A}\cdot\text{g}^{-1}$  over 300 cycles). Wu et al. [31] recently synthesized uniform  $\text{Co}_3\text{V}_2\text{O}_8$  microspheres by a hydrothermal method followed by calcination. The  $\text{Co}_3\text{V}_2\text{O}_8$  microspheres exhibited high cycling stability and rate capability as anode materials owing to the hollow structure, synergistic effects, mechanical stability and their complex chemical composition.

In this work, double-shelled  $\text{Co}_3\text{V}_2\text{O}_8$  hollow nanospheres were fabricated using a solvothermal method followed by a thermal treatment. Scanning electron microscope (SEM) images show that the morphologies of  $\text{Co}_3\text{V}_2\text{O}_8$  nanostructures depend on the annealing temperatures. The formation of the double-shelled hollow nanospheres is the result of interaction between contraction force ( $F_c$ ) and adhesion force ( $F_a$ ) during oxidation. The double-shelled  $\text{Co}_3\text{V}_2\text{O}_8$  hollow nanospheres electrode exhibits an excellent electrochemical performance owing to the benefits of both the double-shell and the hollow morphology, which increases its potential for anode material in the LIBs.

## 2 Experimental

In the experiments, all the analytical grade reagents were used without further purification. First, 20 ml glycerin and 40 mL ethylene glycol were added into a 200-ml glass beaker and stirred for 2 h to form a limpid solution. Then, 3 mmol  $\text{CoCl}_2\cdot\text{H}_2\text{O}$  and 2 mmol vanadyl acetylacetonate ( $\text{VO}(\text{acac})_2$ ) were dissolved in the mixed solution by continuously stirring for 1 h. This solution was transferred into a 100 ml Teflon-lined stainless steel autoclave and heated at  $180 \text{ }^\circ\text{C}$  for 15 h. The obtained product was washed with deionized water thrice and then with anhydrous ethanol and later dried at  $60 \text{ }^\circ\text{C}$  for 12 h. The  $\text{Co}_3\text{V}_2\text{O}_8$  samples were annealed at 350, 450 and  $550 \text{ }^\circ\text{C}$

for 2 h, respectively. The products with different morphologies were marked as double-shelled hollow nanospheres (CVO–DSS), single-shelled hollow nanospheres (CVO–HS) and nanoparticles (CVO–NP), respectively.

X-ray diffraction (XRD; Bruker AXS, D8 diffractometer, Cu  $K\alpha$  radiation) was used to determine the crystal structure of the  $\text{Co}_3\text{V}_2\text{O}_8$  samples. Scanning electron microscope (SEM; JEOLJSM-7400F, Japan), X-ray energy-dispersive spectrometry (EDS; Oxford Instruments, INCA) which was attached to SEM, high-resolution transmission electron microscopy (HRTEM; JEOL-2010) and X-ray photoelectron spectrometer (XPS; VGESCALABMK II spectrometer) were used to detect the morphologies, element compositions and element distributions of these samples. Thermogravimetric analysis (TGA) was performed in air at a heating rate of  $10 \text{ }^\circ\text{C}\cdot\text{min}^{-1}$  from room temperature to  $600 \text{ }^\circ\text{C}$  with an SDT Q600 TA Instruments thermal analyzer.

The  $\text{Co}_3\text{V}_2\text{O}_8$  electrodes were obtained by smearing the mixed slurry (the weight ratio of carboxymethylcellulose sodium, super P and  $\text{Co}_3\text{V}_2\text{O}_8$  sample is 1:1:8) on a Cu foil and dried at  $100 \text{ }^\circ\text{C}$  for 12 h in vacuum. The mass loading of each  $\text{Co}_3\text{V}_2\text{O}_8$  sample was  $\sim 2.6\text{--}2.8 \text{ mg}\cdot\text{cm}^2$ . The assembly of button battery (CR2032-type cells) was arranged in an argon-filled glove box. The separator used was an Celgard 2400 porous polypropylene film, and an electrolyte of  $1 \text{ mol}\cdot\text{L}^{-1}$   $\text{LiPF}_6$  consisting of ethylene carbonate and diethyl carbonate (1: 1 in volume) was used. Galvanostatic charge–discharge tests were conducted with a battery test system (LAND CT2001A, China). The electrochemical impedance spectroscopy (EIS) and cyclic voltammetry (CV) tests were conducted using an electrochemical workstation (CHI 660A).

## 3 Results and discussion

### 3.1 Structure and composition characterization

Figure 1a shows the XRD patterns of the three  $\text{Co}_3\text{V}_2\text{O}_8$  samples. The characteristic peaks at  $2\theta = 35.3^\circ$ ,  $43.5^\circ$ ,  $57.7^\circ$  and  $63.2^\circ$  correspond to the diffraction planes of (122), (042), (025) and (442) for the  $\text{Co}_3\text{V}_2\text{O}_8$  orthorhombic structure (JCPDS No. 74–1487), and no other peaks are observed. Figure 1c shows the XRD pattern of the precursor. The special peak at  $2\theta = 10.8^\circ$  can be attributed to the metal alkoxides of the precursor. The thermogravimetry (TG) curve (Fig. 1b) represents the total precursor weight loss of 31.59%, owing to the evaporation of free water, adsorbed water and the decomposition of organic compounds [32].

XPS measurements were used to analyze the surface chemical composition and valence states of the CVO–DSS

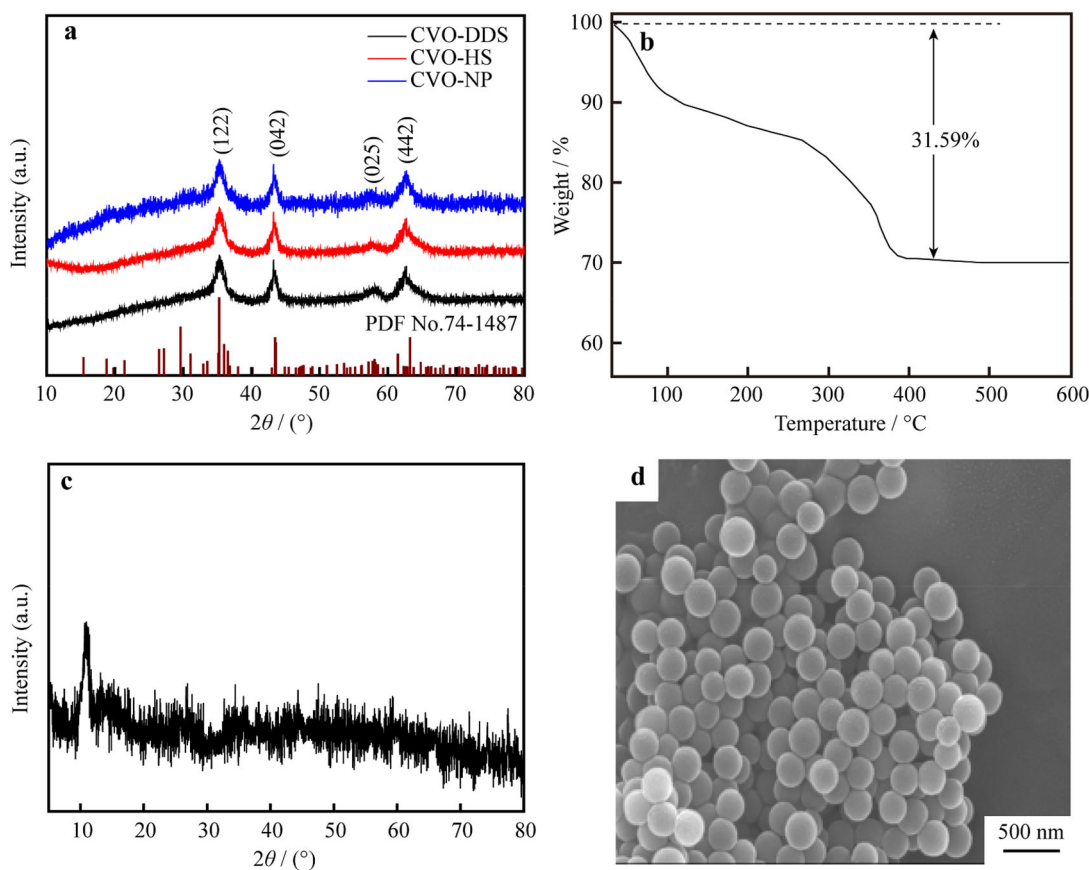


**Fig. 1** **a** XRD patterns of CVO-DSS, CVO-HS and CVO-NP; **b** TGA curves of Co-V-based precursor; **c** XRD pattern and **d** SEM image of Co-V-based precursor

sample. The full spectrum peaks of Co, V and O are shown in Fig. 2a. The XPS spectrum of Co 2p shows two obvious peaks at 780.1 and 796.8 eV, representing Co  $2p_{3/2}$  and Co  $2p_{1/2}$ , respectively, which could be attributed to  $\text{Co}^{2+}$  of the  $\text{Co}_3\text{V}_2\text{O}_8$  sample. The two peaks (783.1 and 798.1 eV) of  $\text{Co}^{3+}$  were located after peak fitting, corresponding to the previous reports [21, 22]. Two other peaks located at 524.7 and 516.9 eV of the V 2p spectrum, allocated to V  $2p_{1/2}$  and V  $2p_{3/2}$ , respectively, correspond to  $\text{V}^{5+}$  of the  $\text{Co}_3\text{V}_2\text{O}_8$  sample, are shown in Fig. 2c. After peak fitting, two peaks of  $\text{V}^{4+}$  were located at 516.7 and 523.8 eV [23]. The O 1s spectrum indicated weak adsorbed-oxygen and doughty lattice-oxygen peaks located at 532.1 and 529.9 eV, respectively, as shown in Fig. 2d. These results confirm successful synthesis of pure  $\text{Co}_3\text{V}_2\text{O}_8$  phase.

### 3.2 Morphology characterization

Figure 3a, b displays the morphology of CVO-DSS sample. The CVO-DSS displays uniform nanosphere morphology with a diameter of  $\sim 600$  nm. The CVO-DSS maintained the nanosphere morphology of the Co-V-based precursor as observed by the SEM (in Fig. 1d). TEM and

HRTEM measurements were used to further examine the microstructures of the  $\text{Co}_3\text{V}_2\text{O}_8$  samples. According to the TEM images (Fig. 3c, d), these nanospheres are of the size 500–800 nm. Strong contrast between the pale center and the dark edges indicates the obvious double-shelled hollow cavity. The HRTEM images, shown in Fig. 3d, e, indicate that the CVO-DSS demonstrates a particular  $d$ -spacing (0.254 nm) of (311) planes. The EDS elemental mapping shown in Fig. 3f confirms the uniform distribution of O, V and Co throughout the CVO-DSS sample. The morphology of the double-shelled  $\text{Co}_3\text{V}_2\text{O}_8$  hollow nanospheres can effectively mitigate the volume change, improve the lithium insertion–extraction and reduce the diffusion distance of  $\text{Li}^+$  [33, 34].

Figure 4 displays the SEM images of the other  $\text{Co}_3\text{V}_2\text{O}_8$  samples (single-shelled hollow  $\text{Co}_3\text{V}_2\text{O}_8$  nanospheres (CVO-HS) and  $\text{Co}_3\text{V}_2\text{O}_8$  nanoparticles (CVO-NP)) obtained at 450 and 550  $^\circ\text{C}$ , respectively. The CVO-HS shown in Fig. 4a, c exhibits single-shelled hollow morphology. However, when the calcination temperature reaches 550  $^\circ\text{C}$ , the as-prepared  $\text{Co}_3\text{V}_2\text{O}_8$  sample (CVO-NP) exhibits the nanoparticles morphology with the size of  $\sim 100$ –300 nm, as shown in Fig. 4b, d. Based on these

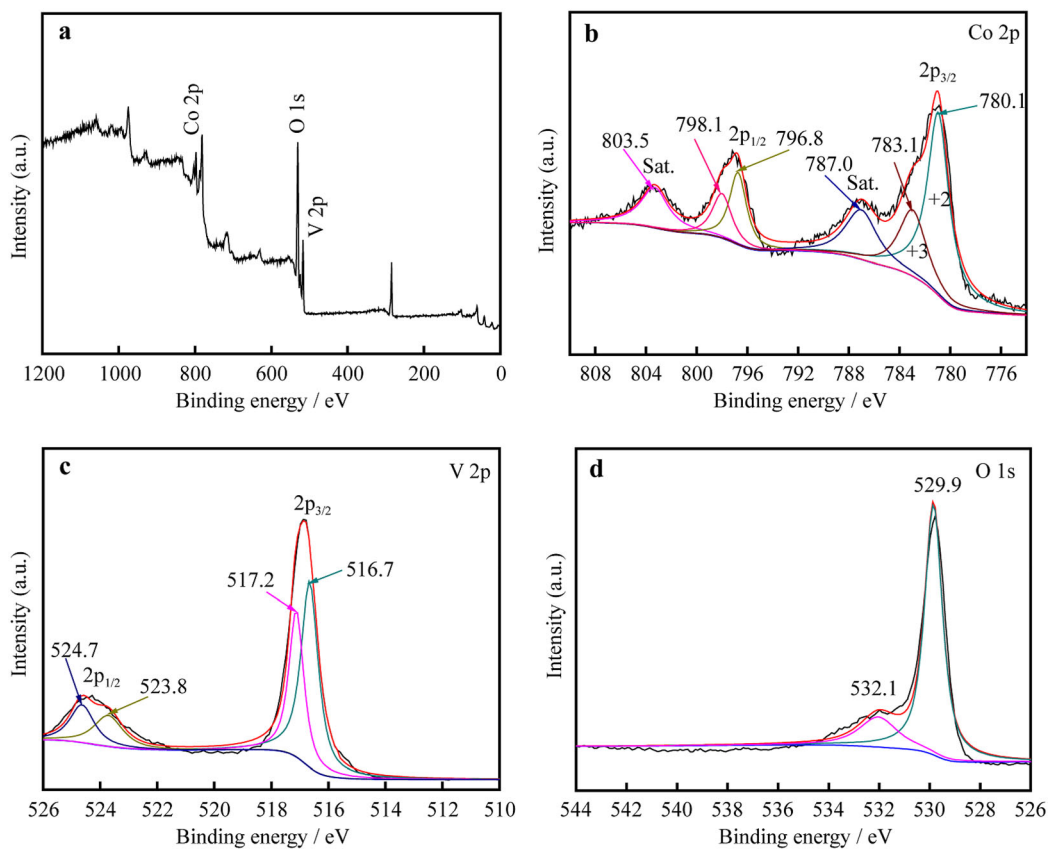


**Fig. 2** XPS spectra of CVO-DSS: **a** survey spectrum, **b** Co 3d, **c** V 2p and **d** O 1s

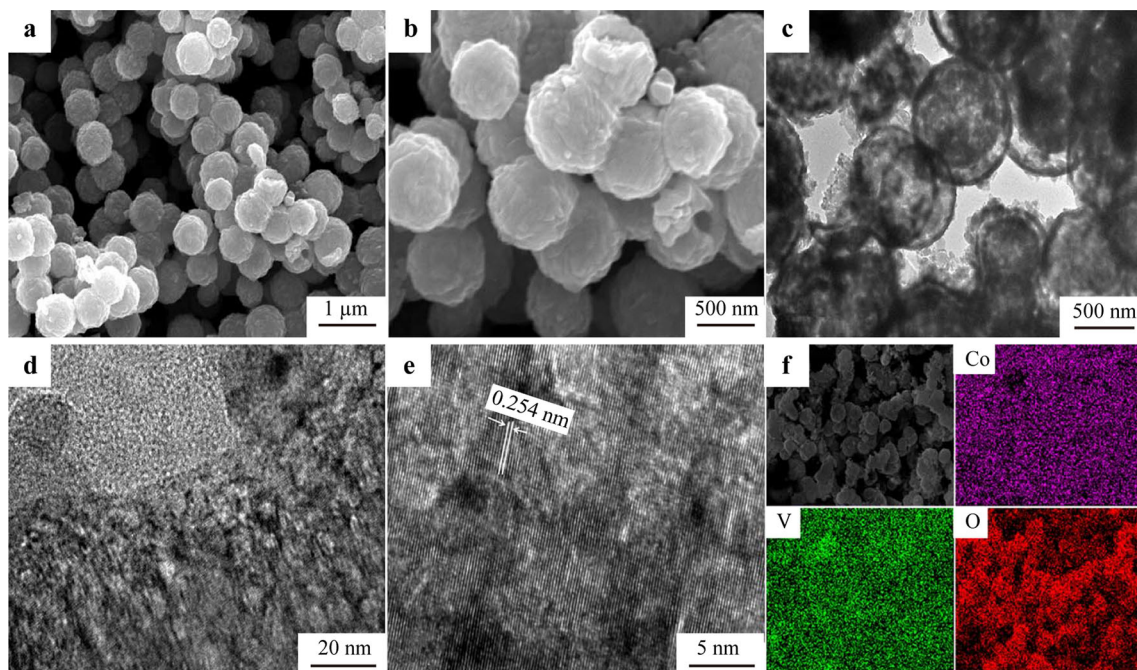


**Fig. 3** **a** and **b** SEM images of CVO-DSS; **c** and **d** low magnification TEM images of CVO-DSS; **e** HRTEM image of CVO-DSS; **f** SEM image and corresponding EDS elemental mappings of Co, V and O of CVO-DSS

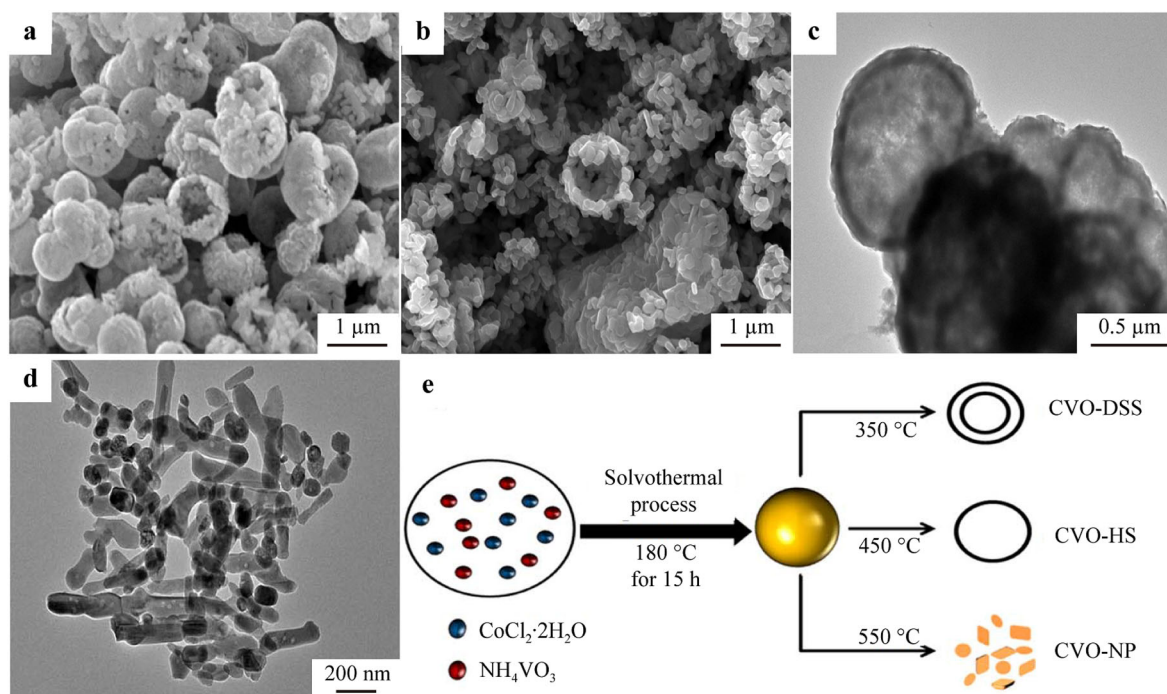


**Fig. 4** SEM images of **a** CVO-HS and **b** CVO-NP; TEM images of **c** CVO-HS and **d** CVO-NP; **e** schematic illustration of temperature-dependent morphologies of  $\text{Co}_3\text{V}_2\text{O}_8$  samples

results and the previous reports, the formation of the double-shelled hollow nanospheres can be considered as the result of the interaction between  $F_c$  and  $F_a$  during oxidation.  $F_c$  can induce an inward shrinkage of the Co-V-based precursor core during the decomposition of the organic species.  $F_a$  prevents the inward contraction of the precursor core. Similar phenomenon has been reported in a variety of nanostructured electrode materials [35–37].

### 3.3 Electrochemical performances

CV curve of the CVO-DSS material was evaluated at a scan rate of  $0.2 \text{ mV}\cdot\text{s}^{-1}$ , as shown in Fig. 5a. For the CVO-DSS electrode, two cathodic peaks at 0.65 and 0.05 V appear in the first intercalation of lithium ions. The peak at 0.65 V can be related to the decomposition of  $\text{Co}_3\text{V}_2\text{O}_8$ . The pristine  $\text{Co}_3\text{V}_2\text{O}_8$  transformed into CoO and the  $\text{Li}_x\text{V}_2\text{O}_5$  resulted from the intercalation of lithium ions into the  $\text{Co}_3\text{V}_2\text{O}_8$  lattice ( $\text{Co}_3\text{V}_2\text{O}_8 + x\text{Li}^+ + xe^- \rightarrow 3\text{CoO} + \text{Li}_x\text{V}_2\text{O}_5$ ). As the insertion of  $\text{Li}^+$  ions increase, the peak at 0.05 V reduces CoO/ $\text{Co}^0$  and the lithiation of  $\text{Li}_x\text{V}_2\text{O}_5$  occurs ( $\text{CoO} + 2\text{Li}^+ + 2e^- \rightarrow \text{Co} + \text{Li}_2\text{O}$ ,  $\text{Li}_x\text{V}_2\text{O}_5 + y\text{Li}^+ + ye^- \rightarrow \text{Li}_{x+y}\text{V}_2\text{O}_5$ ) [38]. During the positive voltage sweep, two peaks at  $\sim 1.31$  and  $2.37$  V may depend on the extraction of lithium ions and hence the oxidation peak does not change in subsequent cycles. However, these cathodic peaks move at  $\sim 1.77$ ,  $1.02$  and  $0.35$  V, respectively. The disappearance of the peak at 0.05 V confirms

the irreversible reaction which can be attributed to the formation and partial disintegration of the SEI layer [39]. The overlapped scanning curves (excluding the first cycle) indicate that the CVO-DSS electrode exhibits reversible discharge/charge process and good stability.

The galvanostatic charge–discharge (GCD) and the cycling performance were evaluated to understand the storage capacity of all the  $\text{Co}_3\text{V}_2\text{O}_8$  electrodes at a current density of  $200 \text{ mA}\cdot\text{g}^{-1}$ , as shown in Fig. 5b, c, d. The first discharge of CVO-DSS reveals a high capacity of  $1366 \text{ mAh}\cdot\text{g}^{-1}$ , and a reversible capacity of  $1192/1210 \text{ mAh}\cdot\text{g}^{-1}$  can be obtained with an ideal coulombic efficiency of 87.3%. After 100 successive cycles, the CVO-DSS electrode indicates a good discharge capacity of  $1210 \text{ mAh}\cdot\text{g}^{-1}$  and a capacity retention of 88.6% compared to the initial discharge capacity, as shown in Fig. 5e. For the CVO-HS and CVO-NP electrodes, the first discharge capacities are  $1311$  and  $1180 \text{ mAh}\cdot\text{g}^{-1}$ , respectively. However, the capacity decay is observed for in the CVO-HS and CVO-NP electrodes. They exhibit the discharge capacities of  $\sim 899$  and  $654 \text{ mAh}\cdot\text{g}^{-1}$  after the 100th cycle, only when the capacity retentions are 68.6% and 55.4% from the first cycle. It is clear that the cycling stability of the CVO-HS and CVO-NP electrodes is inferior to that of the CVO-DSS electrode. It is interesting to observe that the cycling performance of all the  $\text{Co}_3\text{V}_2\text{O}_8$  electrodes increases slightly starting from the second cycle and this repeats until the 45th cycle. Similarly, previous

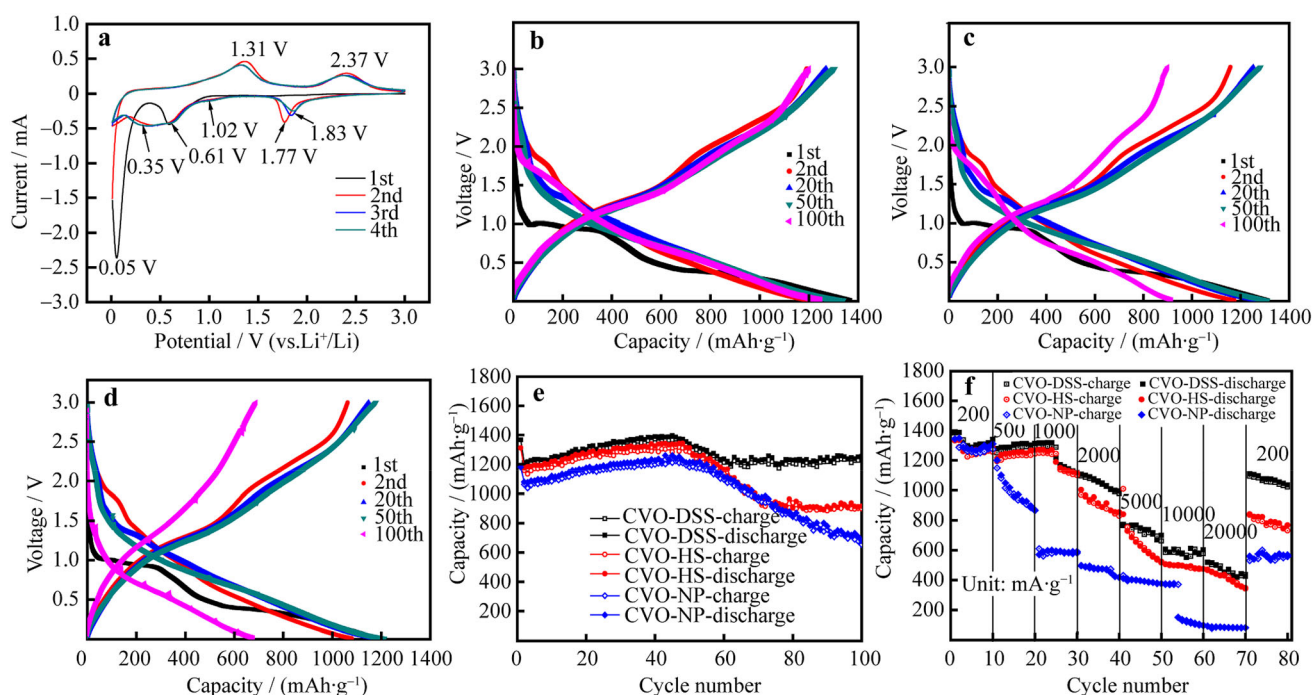


**Fig. 5** a CV curves of CVO-DSS; charge/discharge profiles of b CVO-DSS, c CVO-HS and d CVO-NP; e cycling performance of CVO-DSS, CVO-HS and CVO-NP at a current density of  $200 \text{ mA}\cdot\text{g}^{-1}$ ; f rate performance of CVO-DSS, CVO-HS and CVO-NP

studies on metal oxides reported this phenomenon [25]. The discharge capacities of the CVO-HS and CVO-NP electrodes keep declining with the increase in the number of cycles. The capacity loss of hollow nanosphere and the nanoparticles electrodes could be associated with the pulverization and vigorous volume changes of nanostructures during the charge and discharge process. However, the CVO-DSS remains stable after 100 cycles. This result indicates that the double-shelled hollow nanospheres and porous structure can effectively limit the volume change and pulverization of the electrode materials. Figure 5f shows the rate capabilities of the CVO-DSS, CVO-HS and CVO-NP electrodes. The discharge capacities of 1382, 1278, 1315, 1106, 772, 605 and  $519 \text{ mAh}\cdot\text{g}^{-1}$  can be acquired for the CVO-DSS at 200, 500, 1000, 2000, 5000, 10,000 and 20,000  $\text{mA}\cdot\text{g}^{-1}$ , respectively. More interestingly, when the current density returns to  $200 \text{ mA}\cdot\text{g}^{-1}$ , the reversible capacity of  $1109 \text{ mAh}\cdot\text{g}^{-1}$  can be obtained after 80 cycles. However, the CVO-HS and CVO-NP electrodes display unsatisfactory rate capabilities, especially at high rate.

EIS was utilized to analyze the interfacial property of the three  $\text{Co}_3\text{V}_2\text{O}_8$  electrodes in Fig. 6a. All the Nyquist plots are made up of a semicircles and slanted lines. The diameter of the semicircle represents the ability of charge transfer resistance ( $R_{ct}$ ); the slanted line displays the Warburg resistance ( $Z_w$ ) [40]. From the equivalent circuit in the inset of Fig. 6a ( $R_s$  is the electrolyte resistance), the

$R_{ct}$  value of the CVO-DSS electrode is  $56.3 \Omega$ , which is less than that of the CVO-HS ( $78.5 \Omega$ ) and CVO-NP ( $88.7 \Omega$ ), indicating that the CVO-DSS exhibits a rapid charge transfer and lithium-ion diffusion, compared to the CVO-HS and CVO-NP electrodes. In addition, the linear fitting of the Warburg impedance of all the  $\text{Co}_3\text{V}_2\text{O}_8$  electrodes is shown in Fig. 6b. Lithium-ion diffusion coefficient ( $D_{\text{Li}^+}$ ) is closely related to the slope  $A_w$  of the fitting curve. The slope  $A_w$  affects the ability of lithium-ion diffusion coefficient ( $D_{\text{Li}^+}$ ) [41]. Equation (1) shows the relationship between  $D_{\text{Li}^+}$  and  $A_w$ , and they are inversely proportional to each other [42]. The parameters  $E$  and  $F$  represent the open-circuit voltage and Faraday constant.  $x$ ,  $S$  and  $V_m$  represent the  $\text{Li}^+$  concentration, surface area and molar volume of the active materials in Eq. (1).

$$D_{\text{Li}^+} = 0.5 \left[ \frac{V_m}{FSA_w} \left( -\frac{dE}{dx} \right) \right]^2 \quad (1)$$

The slope  $A_w$  of the CVO-DSS electrode is  $22.6 \Omega\cdot\text{s}^{-1/2}$ , which is less than that of the CVO-HS ( $56.2 \Omega\cdot\text{s}^{-1/2}$ ) and CVO-NP ( $65.3 \Omega\cdot\text{s}^{-1/2}$ ), indicating that the CVO-DSS exhibits rapid lithium-ion diffusion rate, compared to the CVO-HS and CVO-NP electrodes.

To further examine the long-term cycle at high current density, the double-shelled  $\text{Co}_3\text{V}_2\text{O}_8$  hollow nanosphere was tested, as shown in Fig. 7a. Though there is obvious capacity fade above 100 cycles, a satisfying reversible discharge and charge capacity of  $847$  and  $834 \text{ mAh}\cdot\text{g}^{-1}$  can

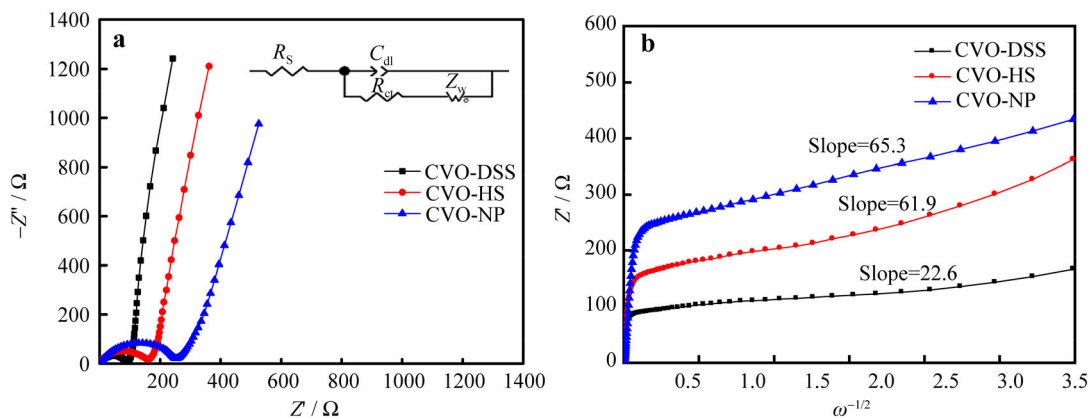


**Fig. 6** **a** EIS and **b** linear fitting of Warburg impedance of CVO-DSS, CVO-HS and CVO-NP ( $Z'$ , real part of impedance;  $Z''$ , imaginary part of impedance)

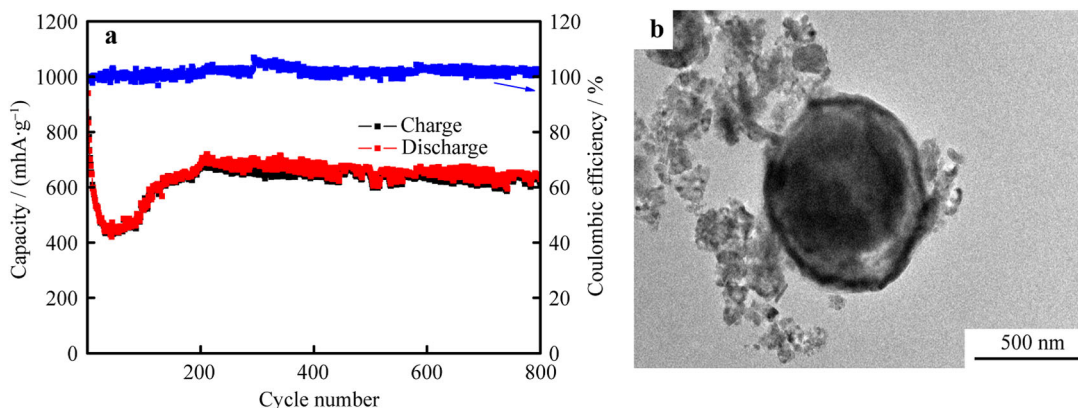


**Fig. 7** **a** Cycling performance of CVO-DSS at current densities of  $5000 \text{ mA}\cdot\text{g}^{-1}$ ; **b** TEM image collected after 100 cycles of CVO-DSS

be achieved. It can also be decreased to 613 and  $628 \text{ mAh}\cdot\text{g}^{-1}$  after 800 consecutive cycles at ultrahigh current density of  $5000 \text{ mA}\cdot\text{g}^{-1}$ . Furthermore, the TEM image of the CVO-DSS electrode after 100 cycles at current densities of  $200 \text{ mA}\cdot\text{g}^{-1}$ , as shown in Fig. 7b, indicating that the CVO-DSS electrode still retains the sphere-like morphology. The CVO-DSS electrode material can retain the morphology even after many cycles, which is the main reasons for its good cyclic stability. Thus, compared to the other existing literature as summarized in Table 1 [21, 24, 26, 27, 30, 31, 34, 43, 44], high lithium storage properties of the CVO-DSS electrode can be attributed to the following: (i) Uniform double-shelled hollow nanospheres effectively reduce the internal resistance and increase the diffusion rate of  $\text{Li}^+$  [45]; (ii) this particular nanostructure efficaciously increases conductivity of the electrode material and buffer the influence of volume expansion [46]; (iii) synergistic effect between Co and V ions can improve the electrochemical performance of the  $\text{Co}_3\text{V}_2\text{O}_8$  electrode material [47].

**Table 1** Comparison of electrochemical performances of  $\text{Co}_3\text{V}_2\text{O}_8$  with previously reported results for LIBs

Samples	Cycles	Rate/ ( $\text{A}\cdot\text{g}^{-1}$ )	Capacity/ ( $\text{mAh}\cdot\text{g}^{-1}$ )
$\text{Co}_3\text{V}_2\text{O}_8$ nanotubes [21]	1100	5.0	630
Porous $\text{Co}_3\text{V}_2\text{O}_8$ microsphere [24]	400	5.0	650
$\text{Co}_3\text{V}_2\text{O}_8$ sponge network [26]	700	1.0	501
$\text{Co}_3\text{V}_2\text{O}_8$ porous nanosheets [27]	1000	3.0	1560
$\text{Co}_3\text{V}_2\text{O}_8$ hollow microsphere [30]	300	10.0	424
$\text{Co}_3\text{V}_2\text{O}_8$ microspheres [31]	400	5.0	550
$\text{Co}_3\text{V}_2\text{O}_8$ hexagonal pyramid [34]	300	0.5	712
$\text{Co}_3\text{V}_2\text{O}_8$ multilayered nanosheets [43]	100	1.0	1114
$\text{Co}_3\text{V}_2\text{O}_8$ nanoparticle [44]	250	0.2	1024
Double-shelled $\text{Co}_3\text{V}_2\text{O}_8$ hollow nanosphere (This work)	800	5.0	628

## 4 Conclusion

In summary, the  $\text{Co}_3\text{V}_2\text{O}_8$  electrode materials with different morphologies (double-shelled hollow nanosphere, single-shelled hollow nanosphere and nanoparticle) were synthesized successfully by using a solvothermal method followed by thermal treatment. The calcination temperature plays a crucial part in the formation of  $\text{Co}_3\text{V}_2\text{O}_8$  particles. The double-shelled  $\text{Co}_3\text{V}_2\text{O}_8$  hollow nanospheres (CVO-DSS) exhibit excellent lithium storage properties with a reversible capacity of  $\sim 1210 \text{ mAh}\cdot\text{g}^{-1}$  at  $200 \text{ mA}\cdot\text{g}^{-1}$  after 100 cycles and also provide  $\sim 628 \text{ mAh}\cdot\text{g}^{-1}$  at  $5000 \text{ mA}\cdot\text{g}^{-1}$  after 800 cycles. The double-shelled hollow nanosphere provides several advantages like increasing the  $\text{Li}^+$  diffusion coefficient and electronic conductivity, decreasing the electrode polarization and simultaneously balancing the volume expansion of  $\text{Co}_3\text{V}_2\text{O}_8$  during the cycling.

**Acknowledgements** This study was financially supported by the National Natural Science Foundation of China (No. 21476063), Guizhou Provincial Education Department (No. KY [2018] 031), the Project of Hubei Provincial Science & Technology Department (No. 2018ACA147) and the Open-End Fund for Hubei Key Laboratory of Pollutant Analysis & Reuse Technology (No. PA200104). H. Zheng acknowledges the China Scholarship Council (CSC) for scholarship support.

## References

- Chen WS, Yu HP, Lee SY, Wei T, Li J, Fan ZJ. Nanocellulose: a promising nanomaterial for advanced electrochemical energy storage. *Chem Soc Rev*. 2018;47(8):2837.
- Jiang J, Li YY, Liu JP, Huang XT, Yuan CZ, Lou XW. Recent advances in metal oxide-based electrode architecture design for electrochemical energy storage. *Adv Mater*. 2012;24(38):5166.
- Larcher D, Tarascon JM. Towards greener and more sustainable batteries for electrical energy storage. *Nat Chem*. 2015;7(1):19.
- Dunn B, Kamath H, Tarascon JM. Electrical energy storage for the grid: a battery of choices. *Science*. 2011;334(6058):928.
- Yang Z, Zhang J, Kintner-Meyer MCW, Lu X, Choi D, Lemmon JP, Liu J. Electrochemical energy storage for green grid. *Chem Rev*. 2011;111(5):3577.
- Lu Y, Yu L, Wu MH, Wang Y, Lou XW. Construction of complex  $\text{Co}_3\text{O}_4@ \text{Co}_3\text{V}_2\text{O}_8$  hollow structures from metal-organic frameworks with enhanced lithium storage properties. *Adv Mater*. 2018;30(1):1702875.
- Yang J, Wu MQ, Gong F, Feng TT, Chen C, Liao JX. Facile and controllable synthesis of solid  $\text{Co}_3\text{V}_2\text{O}_8$  micro-pencils as a highly efficient anode for Li-ion batteries. *RSC Adv*. 2017;7(39):24418.
- Li L, Seng KH, Feng CQ, Liu HK, Guo ZP. Synthesis of hollow  $\text{GeO}_2$  nanostructures, transformation into  $\text{Ge}@ \text{C}$  and lithium storage properties. *J Mater Chem A*. 2013;1(26):7666.
- Li D, Wang HQ, Liu HK, Guo ZP. A new strategy for achieving a high performance anode for lithium ion batteries-encapsulating germanium nanoparticles in carbon nanoboxes. *Adv Energy Mater*. 2016;6(5):1501666.
- Li J, Yang JY, Wang JT, Lu SG. A scalable synthesis of silicon nanoparticles as high-performance anode material for lithium-ion batteries. *Rare Met*. 2019;38(3):199.
- Ji YR, Weng ST, Li XY, Zhang QH, Gu L. Atomic-scale structural evolution of electrode materials in Li-ion batteries: a review. *Rare Met*. 2020;39(3):205.
- Zhang GQ, Lou XW. General synthesis of multi-shelled mixed metal oxide hollow spheres with superior lithium storage properties. *Angew Chem Int Ed*. 2014;126(34):9187.
- Wang JL, Pei J, Hua K, Chen DH, Jiao Y, Hu YY, Chen G. Synthesis of  $\text{Co}_2\text{V}_2\text{O}_7$  hollow cylinders with enhanced lithium storage properties using  $\text{H}_2\text{O}_2$  as an etching agent. *Chem Electro Chem*. 2018;5(5):737.
- Zheng H, Zhang Q, Gao H, Sun W, Zhao HM, Feng CQ, Mao JF, Guo ZP. Synthesis of porous  $\text{MoV}_2\text{O}_8$  nanosheets as anode material for superior lithium storage. *Energy Storage Mater*. 2019;22:128.
- Gan LH, Deng DR, Zhang YJ, Li G, Wang XY, Jiang L, Wang CR.  $\text{Zn}_3\text{V}_2\text{O}_8$  hexagon nanosheets: a high-performance anode material for lithium-ion batteries. *J Mater Chem A*. 2014;2(8):2461.
- Sim DH, Rui XH, Chen J, Tan HT, Lim TM, Yazami R, Hng HH, Yan QY. Direct growth of  $\text{FeVO}_4$  nanosheet arrays on stainless steel foil as high-performance binder-free Li ion battery anode. *RSC Adv*. 2012;2(9):3630.
- Zhang L, Zhao KN, Luo YZ, Dong YF, Xu WW, Yan MY, Ren WH, Zhou L, Qu LB, Mai LQ. Acetylene black induced heterogeneous growth of macroporous  $\text{CoV}_2\text{O}_6$  nanosheet for high-rate pseudocapacitive lithium-ion battery anode. *ACS Appl Mater Interfaces*. 2016;8(11):7139.
- Lv C, Sun JX, Chen G, Yan CS, Chen DH. Achieving  $\text{Ni}_3\text{V}_2\text{O}_8$  amorphous wire encapsulated in crystalline tube nanostructure as anode materials for lithium ion batteries. *Nano Energy*. 2017;33:138.
- Yin ZG, Qin JW, Wang W, Cao MH. Rationally designed hollow precursor-derived  $\text{Zn}_3\text{V}_2\text{O}_8$  nanocages as a high-performance anode material for lithium-ion batteries. *Nano Energy*. 2017;31:367.
- Lu Y, Nai JW, Lou XW. Formation of  $\text{NiCo}_2\text{V}_2\text{O}_8$  yolk-double shell spheres with enhanced lithium storage properties. *Angew Chem Int Ed*. 2018;57(11):2899.
- Qin ZZ, Pei J, Chen G, Chen DH, Hu YY, Lv C, Bie CF. Design and fabrication of  $\text{Co}_3\text{V}_2\text{O}_8$  nanotubes by electrospinning as a high-performance anode for lithium-ion batteries. *New J Chem*. 2017;41(13):5974.
- Gong F, Xia DW, Bi C, Yang J, Zeng W, Chen C, Ding YL, Xu ZQ, Liao JX, Wu MQ. Systematic comparison of hollow and solid  $\text{Co}_3\text{V}_2\text{O}_8$  micro-pencils as advanced anode materials for lithium ion batteries. *Electrochim Acta*. 2018;264:358.
- Gao GX, Lu SY, Dong BT, Xiang Y, Xi K, Ding SJ. Mesoporous  $\text{Co}_3\text{V}_2\text{O}_8$  nanoparticles grown on reduced graphene oxide as a high-rate and longlife anode material for lithium-ion batteries. *J Mater Chem A*. 2016;4(17):6264.
- Sambandam B, Soundharrajan V, Mathew V, Song JJ, Kim SJ, Jo J, Tung DP, Kim S, Kim J. Metal-organic framework-combustion: a new, cost-effective and one-pot technique to produce a porous  $\text{Co}_3\text{V}_2\text{O}_8$  microsphere anode for high energy lithium ion batteries. *J Mater Chem A*. 2016;4(38):14605.
- Wu FF, Xiong SL, Qian YT, Yu SH. Hydrothermal synthesis of unique hollow hexagonal prismatic pencils of  $\text{Co}_3\text{V}_2\text{O}_8 \cdot n\text{H}_2\text{O}$ : a new anode material for lithium-ion batteries. *Angew Chem*. 2015;54(37):10787.
- Yang GZ, Cui H, Yang GW, Wang CX. Self-assembly of  $\text{Co}_3\text{V}_2\text{O}_8$  multilayered nanosheets: controllable synthesis, excellent Li-storage properties and investigation of electrochemical mechanism. *ACS Nano*. 2014;8(5):4474.



- [27] Zhang Q, Pei J, Chen G, Bie CF, Sun JX, Liu J. Porous  $\text{Co}_3\text{V}_2\text{O}_8$  nanosheets with ultrahigh performance as anode materials for lithium ion batteries. *Adv Mater Interfaces*. 2017;4(13):1700054.
- [28] Hou LR, Bao RQ, Zhang YR, Sun X, Zhang JY, Dou H, Zhang XG, Yuan CZ. Structure-designed synthesis of yolk-shell hollow  $\text{ZnFe}_2\text{O}_4/\text{C}@\text{N}$ -doped carbon sub-microspheres as a competitive anode for high-performance Li-ion batteries. *J Mater Chem A*. 2018;6(37):17947.
- [29] Wang PX, Zhang Y, Yin YY, Fan LS, Zhang NQ, Sun KN. Anchoring hollow  $\text{MoO}_2$  spheres on graphene for superior lithium storage. *Chem Eng J*. 2018;334:257.
- [30] Luo YZ, Xu X, Tian XC, Wei QL, Yan MY, Zhao KG, Xua XM, Mai LQ. Facile synthesis of a  $\text{Co}_3\text{V}_2\text{O}_8$  interconnected hollow microsphere anode with superior high-rate capability for Li-ion batteries. *J Mater Chem A*. 2016;4(14):5075.
- [31] Wu MQ, Yang J, Chen C, Feng TT, Gong F, Liao JX. Uniform  $\text{Co}_3\text{V}_2\text{O}_8$  microspheres via controllable assembly for high-performance lithium-ion battery anodes. *New J Chem*. 2018;42(7):4881.
- [32] Wu MZ, Zhang XF, Gao S, Cheng XL, Rong ZM, Xu YM, Zhao H, Huo LH. Construction of monodisperse vanadium pentoxide hollow spheres via a facile route and triethylamine sensing property. *CrystEngComm*. 2013;15(46):10123.
- [33] Deng JJ, Yu XL, Qin XY, Liu BL, He YB, Li BH, Kang FY. Controlled synthesis of anisotropic hollow  $\text{ZnCo}_2\text{O}_4$  octahedrons for high-performance lithium storage. *Energy Storage Mater*. 2018;11:184.
- [34] Wang YH, Wu BH, He XY, Zhang YY, Li H, Peng YY, Wang J, Zhao JB. Synthesis of micro/nanostructured  $\text{Co}_9\text{S}_8$  cubes and spheres as high performance anodes for lithium ion batteries. *Electrochim Acta*. 2017;230:299.
- [35] Jin J, Wu L, Huang SZ, Yan M, Wang HG, Chen LH, Hasan T, Li Y, Su BL. Hierarchy design in metal oxides as anodes for advanced lithium-ion batteries. *Small Methods*. 2018;2(11):1800171.
- [36] Yu L, Yu XY, Lou XW. The design and synthesis of hollow micro-/nanostructures: present and future trends. *Adv Mater*. 2018;30(38):1800939.
- [37] Shen LF, Yu L, Yu XY, Zhang XG, Lou XW. Self-templated formation of uniform  $\text{NiCo}_2\text{O}_4$  hollow spheres with complex interior structures for lithium-ion batteries and supercapacitors. *Angew Chem Int Ed*. 2015;54(6):1868.
- [38] Gong F, Xia DW, Zhou Q, Liao JX, Wu MQ. Novel spherical cobalt/nickel mixed-vanadates as high-capacity anodes in lithium ion batteries. *J Alloy Compd*. 2018;766:442.
- [39] Pan A, Wang Y, Xu W, Nie Z, Liang S, Nie Z, Wang C, Cao G, Zhang JG. High-performance anode based on porous  $\text{Co}_3\text{O}_4$  nanodiscs. *J Power Sources*. 2014;255:125.
- [40] Wu FX, Maier J, Yu Y. Guidelines and trends for next-generation rechargeable lithium and lithium-ion batteries. *Chem Soc Rev*. 2020;49(5):1569.
- [41] Liu XL, Cao YC, Zheng H, Chen X, Feng CQ. Synthesis and modification of  $\text{FeVO}_4$  as novel anode for lithium-ion batteries. *Appl Surf Sci*. 2017;394:183.
- [42] Zhang Q, Pei J, Chen G, Bie CF, Chen DH, Jiao Y, Rao JC.  $\text{Co}_3\text{V}_2\text{O}_8$  hexagonal pyramid with tunable inner structure as high performance anode materials for lithium ion battery. *Electrochim Acta*. 2017;238:227.
- [43] Soundharajan V, Sambandam B, Song J, Kim S, Jo J, Kim S, Lee S, Mathew V, Kim J.  $\text{Co}_3\text{V}_2\text{O}_8$  sponge network morphology derived from metal-organic framework as an excellent lithium storage anode material. *ACS Appl Mater Interfaces*. 2016;8(13):8546.
- [44] Soundharajan V, Sambandam B, Song JJ, Kim SJ, Jo J, Duong PT, Kim S, Mathew V, Kim J. Facile green synthesis of a  $\text{Co}_3\text{V}_2\text{O}_8$  nanoparticle electrode for high energy lithium-ion battery applications. *J Colloid Inter Sci*. 2017;501:133.
- [45] Liu N, Wu H, McDowell MT, Yao Y, Wang CM, Cui Y. A yolk-shell design for stabilized and scalable Li-ion battery alloy anodes. *Nano Lett*. 2012;12(6):3315.
- [46] Liu J, Qiao SZ, Chen JS, Lou XW, Xing XR, Lu GQ. Yolk/shell nanoparticles: new platforms for nanoreactors, drug delivery and lithium-ion batteries. *Chem Commun*. 2011;47:12578.
- [47] Lu Y, Yu L, Lou XW. Nanostructured conversion-type anode materials for advanced lithium-ion batteries. *Chem*. 2018;4(5):972.